Highly Stable Halide-Electrolyte-Based All-Solid-State Li–Se Batteries

Xiaona Li, Jianwen Liang, Jung Tae Kim, Jiamin Fu, Hui Duan, Ning Chen, Ruying Li, Shangqian Zhao, Jiantao Wang, Huan Huang, and Xueliang Sun*

Solid-state Li–S and Li–Se batteries are promising devices that can address the safety and electrochemical stability issues that arise from liquid-based systems. However, solid-state Li–Se/S batteries usually present poor cycling stability due to the high resistance interfaces and decomposition of solid electrolytes caused by their narrow electrochemical stability windows. Here, an integrated solid-state Li–Se battery based on a halide Li_3HoCl_6 solid electrolyte with high ionic conductivity is presented. The intrinsic wide electrochemical stability window of the Li_3HoCl_6 and its stability toward Se and the lithiated species effectively inhibit degeneration of the electrolyte and the Se cathode by suppressing side reactions. The inherent thermodynamic mechanism of the lithiation/delithiation process of the Se cathode in solid is also revealed and confirmed by theoretical calculations. The battery achieves a reversible capacity of 402 mAh g^{-1} after 750 cycles. The electrochemical performance, thermodynamic lithiation/delithiation mechanism, and stability of metal-halide-based Li–Se batteries confer theoretical study and practical applicability that extends to other energy-storage systems.

1. Introduction

The performance and application of lithium batteries are dictated by the electrochemical behavior and reversibility of their electrodes for accommodating Li^+. In particular, the electrochemical behavior of electrodes, the cycle life, and the safety of batteries highly depends on the electrolyte system. The electrolyte strongly influences the formation of the electrode–electrolyte interface and its features and also affects the lithiation/delithiation process of the electrodes. A typical example can be given by Li metal batteries (such as Li–S and Li–Se batteries) involving chalcogen-based cathodes. Like S cathodes, the electrolyte-dependent (including solvents and lithium salt) lithiation/delithiation behaviors of Se cathodes have been extensively verified.[1–3]

In carbonate electrolytes, Se cathodes have been shown to exhibit single-phase transformation between Se and Li_2Se, however, this mechanism remains controversial as several works have presented a multiphase conversion process when using a different electrolyte.[4,5] Though the interface formed on Se-based cathodes has shown to be efficient in facilitating electrode kinetics, the serious side reaction which occurs between lithiated species and the electrolyte cannot be ignored, as they greatly influence the lithiation mechanism and results in safety concerns. For example, Li_2Se reacts strongly with lithium salt in the organic electrolyte such as $LiPF_6$ (**Figure 1**). In ether electrolytes, Se cathodes present multiphase transformation between Se and Li_2Se through the formation of polyselenide intermediates.[6] In this system, major challenges arise from the dissolution of polyselenide intermediates, which leads to loss of Se and the consequent corrosion of the Li anode during cycling due to the shuttle effect. The electrolyte-dependent lithiation/delithiation behavior of the Se cathode stems from the physical/chemical properties of the organic electrolytes, such as solubility and reactivity, which results in a highly complex and unsafe Li–Se battery system that meet commercial standards.[7–9]

Inspired by the advantages of the solid-state system, all-solid-state Li–Se batteries based on sulfide solid-state electrolytes (SSEs) have been reported.[10,11] The solid-state system has shown to be effective in avoiding the dissolution and side reactions caused by the lithiated intermediates, demonstrating improved cycling stability. Despite this, the large amount of carbon additives trigger SSE degradation in the applied voltage range for all-solid-state Li–Se batteries (1.0–3.0 V, vs Li^+/Li) due to the limited electrochemical stability windows of sulfide SSEs (≈1.7–2.3 V, vs Li^+/Li).[12,13] Moreover, the observed electrochemical behavior is more than that of $Se + 2Li^+ + 2e^- \rightleftharpoons Li_2Se$ since the redox activity of the thiophosphate units overlaps with

X. Li, J. Liang, J. T. Kim, J. Fu, H. Duan, R. Li, X. Sun
Department of Mechanical and Materials Engineering
University of Western Ontario
1151 Richmond St, London, Ontario N6A 3K7, Canada
E-mail: xsun9@uwo.ca

J. Liang, S. Zhao, J. Wang
China Automotive Battery Research Institute Co. Ltd
5th Floor, No. 43, Mining Building, North Sanhuan Middle Road
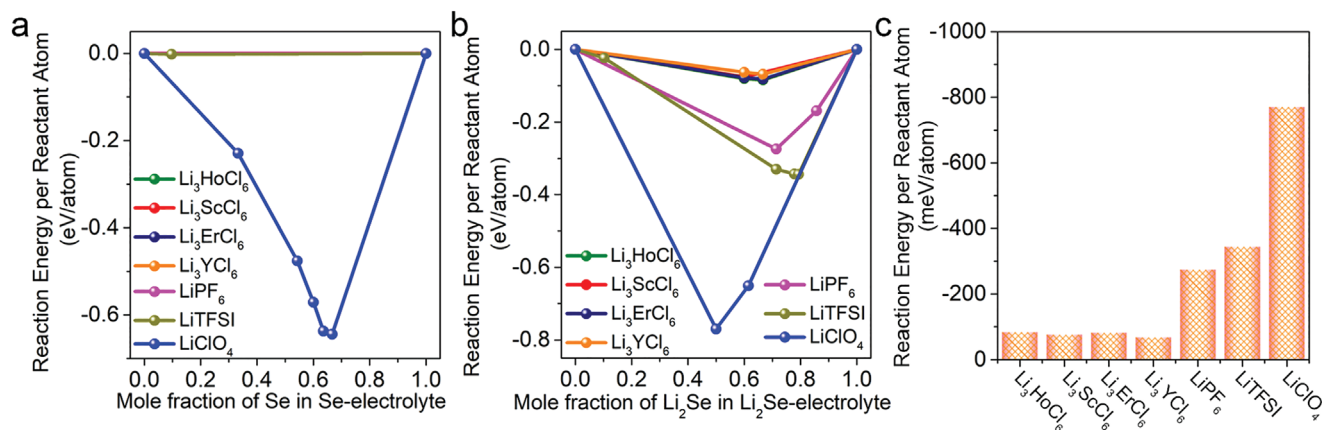Beijing 100088, China

N. Chen
Canadian Light Source
44 Innovation Boulevard, Saskatoon SK S7N 2V3, Canada

H. Huang
Glabat Solid-State Battery Inc.
700 Collip Circle, London, ON N6G 4X8, Canada

The ORCID identification number(s) for the author(s) of this article can be found under https://doi.org/10.1002/adma.202200856.

**ADVANCED
SCIENCE NEWS**
www.advancedsciencenews.com

**ADVANCED
MATERIALS**
www.advmat.de

Figure 1. Compatibility between Se or lithiated selenium and halide SSEs as well as lithium salts in liquid electrolytes. a) Calculated reaction energy between Se and typical halide SSEs as well as lithium salts as a function of mixing ratio. b) Calculated reaction energy between Li_2Se and typical halide SSEs as well as lithium salts as a function of mixing ratio. c) Comparison of the highest reaction energy between Li_2Se and typical halide SSEs as well as lithium salts.

that of elemental Se to some extent.[14–16] The narrow electrochemical windows of sulfide SSEs and serious side reactions which occur from the degradation of sulfide SSEs deeply affect the lithiation/delithiation process of Se cathode and lead to an elusive reaction mechanism and inherent safety concerns.

Recently, halide-based SSEs have gained continuous research interest due to their high ionic conductivity, feasible synthesis methods, and wide electrochemical windows. By optimizing the synthesis method (Li_3YCl_6,[17] Li_3InCl_6,[18] Li_2ZrCl_6[19]), tuning the composition or structure (Li_3ScCl_6,[20,21] Zr doped Li_3MCl_6 [M = Y, Er],[22] $Li_{2.25}Zr_{0.75}Fe_{0.25}Cl_6$,[23] $Li_{2.6}Yb_{0.6}Hf_{0.4}Cl_6$,[24] and $Li_{2.7}Yb_{0.7}Zr_{0.3}Cl_6$[25]), and reducing the grain boundary resistance ($Li_3Y(Br_3Cl_3)$), the room-temperature conductivity of halide SSEs can be as high as 7.2×10^{-3} S cm^{-1} until now.[26] Halide SSEs can even be synthesized by a facile wet-chemistry method using water as a solvent.[27,28] Furthermore, halide SSEs, especially chlorides and fluorides, exhibit wide electrochemical windows among all types of SSEs, which have been proven by theoretical[12,29] and experimental[30,31] studies. Until now, all the solid-state batteries in the halide SSEs system are still focused on traditional oxide cathodes.[17,19,25,31,32] While there have been predictions that halide SSEs can be used to explore the reversible storage of Li$^+$ into new compounds other than oxide cathodes.

Herein, we tame the side reactions between the electrolyte and Se cathode or Li_xSe_y species during cycling by using a halide Li_3HoCl_6 solid electrolyte with high ionic conductivity in an all-solid-state Li–Se battery system. An intrinsic thermodynamic mechanism of the lithiation/delithiation process of Se cathode in the solid system was revealed, owing to the wide electrochemical window and high stability of Li_3HoCl_6 electrolyte. The battery has a reversible capacity of 402 mAh g^{-1} after 750 cycles. The integration of the Li–Se battery systems focuses on the intrinsic chemical stability, which has advantages over the additional modification processes mentioned above. The mechanism and the corresponding impact of our findings enrich the fundamental understanding of the lithiation/delithiation mechanism of the Se cathode in solid and constitute a crucial step in the design of novel battery systems with tunable

properties for a wide range of applications including Li–S batteries and beyond.

2. Results and Discussion

To evaluate the availability of Li_3MCl_6 SSEs in the Li–Se battery system, the stability between Li_3MCl_6 SSEs (M = Ho, Sc, Er, Y) and Se cathode as well as the possible lithiated products should be considered. Thus, the stability of Li_3MCl_6 SSEs with the Se cathode and possible lithiated materials (Li_2Se_8, Li_2Se_6, Li_2Se_4, Li_2Se_2, and Li_2Se) is first studied by calculating the mutual reaction energy, and the results are shown in Figure 1 and Figure S1, Supporting Information. It can be seen that Se does not react with all the Li_3MCl_6 SSE as the calculated energy is 0. Furthermore, the reaction energies of Li_3MCl_6 SSEs with all possible lithiated materials are only about ≈41–84 meV per atom (Figure 1b and Figure S1, Supporting Information). The relatively low mutual reaction energy of less than 100 meV per atom indicates good stability of the Li_3MCl_6 SSEs with all lithiated materials. It should be noted that such a value is much lower than the reaction energy between lithiated selenium species and traditional lithium salts (such as $LiPF_6$, LiTFSI, and $LiClO_4$) that are used in liquid electrolytes (Figure 1b,c), which exhibits as high as several hundred meV per atom. Furthermore, it has been reported that the Li_3MCl_6 SSEs possess wide electrochemical stability windows (such as 0.64–4.25 V for Li_3HoCl_6, 0.62–4.21 V for Li_3YCl_6, and 0.87–4.21 V for Li_3ScCl_6 vs Li$^+$/Li).[12,29,33] Thus, those Li_3MCl_6 SSEs in cathode composites will not decompose even with a large amount of conductive carbon additives within the applied voltage for all-solid-state Li–Se cells (1–3 V vs Li$^+$/Li). Moreover, the real electrochemical behavior of the active Se cathode can be revealed since there is no possible overlapped lithiation/delithiation process originating from Li_3MCl_6 SSEs. All the results demonstrate that Li_3MCl_6 SSEs are suitable electrolytes for Li–Se cells as the challenges include poor stability with Se cathode (as well as lithiated species), the SSEs degradation problems, and the resultant poor Li$^+$ transport issues will be avoided for the halide-based all-solid-state Li–Se battery systems.

The Se–Li$_3$HoCl$_6$ (Se–LHC) composite was first prepared by a typical ball milling process using Se and Li$_3$HoCl$_6$ (weight ratio 1:1) to evaluate the charge transfer resistance. Detailed information of the synthesized Li$_3$HoCl$_6$ (RT ionic conductivity of 1.05×10^{-3} S cm^{-1}, Figure S2, Supporting Information) can be found in the Supporting Information. Figure S3, Supporting Information, shows the impedance spectroscopy and corresponding equivalent circuit of the Se–LHC composite. The results show that the total conductivity (σ_{total}, including both Li$^+$ and electron migration) of Se–LHC is $\approx3.8 \times 10^{-5}$ S cm^{-1}. The electronic conductivity ($\sigma_{electron}$) of Se–LHC which is determined by the steady-state current response at different applied voltages is about 1.4×10^{-5} S cm^{-1} (Figure S4, Supporting Information), which is slightly lower than that of commercial Se powder (2.5×10^{-5} S cm^{-1}, Figure S5, Supporting Information). The results indicate that the Li$^+$ conductivity (σ_{Li+}) of Se–LHC composite should be in the same order of $\sigma_{electron}$, which means that the Se–LHC composite is highly mixed conductive, and the Li$^+$/electron conductivity is much higher than that in the sulfide system, especially the electronic conductivity (3×10^{-8} S cm^{-1} for Se–Li$_3$PS$_4$).[10] Thus, the amount of carbon additive in the Se–Li$_3$HoCl$_6$–C (Se–LHC–C) cathode composite is reduced to 9.09 wt% compared to traditional 20 wt% (or more) in solid-state systems used in previous reports.[10,11,34,35]

The all-solid-state Li–Se cells with Se–LHC–C (typical scanning electron microscopy images shown in Figure S6, Supporting Information) cathode composites were prepared and cycled with a cut-off potential of 1.0–3.0 V versus Li$^+$/Li. Due to the instability of Li$_3$HoCl$_6$ toward the Li anode, a thin layer of commercial Li$_6$PS$_5$Cl was placed between the Li$_3$HoCl$_6$ SSE and the Li anode since the negligible interfacial ion transport resistance between sulfide and halide electrolytes.[36,37] More efforts to overcome the instability toward Li metal for halide SSEs are highly desirable while not the focus of this study. The detailed fabrication procedure of the cells can be found in the Supporting Information. The impedance spectra of the assembled all-solid-state Li–Se cells at a steady state remain unchanged (Figure S7, Supporting Information), indicating the stable interfaces of the cell. To further check the redox inertness of Li$_3$HoCl$_6$ within the cathode composites, the all-solid-state cells containing Li$_3$HoCl$_6$–C composite (same mass ratio as that of Se–LHC–C) were also prepared and cycled within the same potential range. It can be seen that there is no reversible capacity of Li$_3$HoCl$_6$–C composites (Figure S8, Supporting Information), which demonstrates that the Li$_3$HoCl$_6$ SSE neither decomposes nor influences the electrochemical behavior of Se. The stability of the Li$_3$HoCl$_6$ SSE during cycling and the compatibility of the Li$_3$HoCl$_6$ SSE toward the Se cathode as well as the lithiated species were proven by X-ray absorption near edge structure (XANES) analysis. All the Ho L$_3$-edge XANES spectra of the Se–LHC–C cathode composite at different discharge/charge states (Figure S9, Supporting Information) possess the same position and shape, indicating that the chemical state of Ho is similar with no observable change.

The reversible capacity of the all-solid-state Li–Se cell is 617 mAh g^{-1} at 50 mA g^{-1} (0.1 C). The cell exhibits two discharge plateaus at ≈2.0 and 1.95 V as presented in **Figure 2**a, and the stepwise lithiation process for Se cathode was further reflected from the two apparent sharp reduction peaks at ≈2.0 and 1.91 V

in the corresponding dQ/dV profiles (Figure 2b). Thus, the electrochemical behavior of the Se cathode in halide-based cells is different from those obtained in cells using conventional liquid electrolytes (carbonate or ether).[1,5] Moreover, the discharge/charge curves also show a considerably low overpotential of about 0.3 V, which is much smaller than the case with sulfide SSE (Figure S10, Supporting Information), implying the facile kinetics and fast charge carrier transport within the cathode composites of Li–Se cells with Li$_3$HoCl$_6$ SSE. The overpotential is much lower than that in the all-solid-state Li–S batteries (≈0.7 V in the sulfide-based system),[38,39] further demonstrating the feasible conversion reaction in halide-based all-solid-state Li–Se cells. In addition, it should be noted that the unique two-plateaus lithiation mechanism is universal for halide SSEs with an appropriate electrochemical stability window. For example, the Se–Li$_3$ScCl$_6$–C cathode also presented similar discharge/charge curves (Figure S11, Supporting Information) as that of the Se–LHC–C cathode.

The lithiation/delithiation behavior of the Se cathode in other electrolytes is also compared in Figure S12, Supporting Information. The electrochemical behavior of Se is highly dependent on the electrolyte system. The majority of reports show typical one-step lithiation for the Se cathode in carbonate-based electrolytes (Figure S12a, Supporting Information), while multiple lithiation steps occur via the intermediates of Li$_2$Se$_x$ in ether-based electrolytes (Figure S12b, Supporting Information). In the sulfide Li$_3$PS$_4$ system, direct conversion between Se and Li$_2$Se was disclosed. Moreover, the lithiation/delithiation of a small portion of interfacial PS$_{4-x}$Se$_x^{3-}$ species was also detected (Figure S12c, Supporting Information).[10] However, it is important to note that the lithiation/delithiation of sulfide SSEs within the Se–Li$_3$PS$_4$–C cathode composite was not excluded, which means that the discharge/charge plateaus and reversible capacity cannot be solely attributed to the Se cathode.[10]

The Raman spectra of commercial Se, Li$_3$HoCl$_6$, and Se–LHC–C composite were presented in Figure S13, Supporting Information. The commercial Se displays a typical peak at 237 cm^{-1} due to the crystallites of the trigonal Se.[40] However, the Se–LHC–C composite presents a broad band at 254 cm^{-1} mainly due to the amorphous Se chains,[40] which indicates that the crystalline state of Se is destroyed after the ball-milling process, while it still maintains the chain structure. The amorphous state of the Se–LHC–C composite is further confirmed by the X-ray diffraction result shown in Figure S14, Supporting Information. The evolution of the Raman spectra upon lithiation/delithiation process of Se–LHC–C cathode was recorded to reveal its lithiation mechanism (Figure 2c,d). The in situ measurements show that the Raman peak of Se chains fades quickly as soon as lithiation starts, indicating the destruction of the chain structure. Then such peak weakens gradually in intensity until with almost no remaining intensity at the end of the lithiation process. On delithiation the peak return to its initial position, but with relatively weakened intensity. The other peak at 237 cm^{-1} was also detected, demonstrating the partial crystallization of the Se after the redelithiation process.

The impedance spectra of the all-solid-state Li–Se cell during the first discharge/charge cycle were shown in **Figure 3**a,d. It can be seen that the resistance gradually increased during the discharge process, which originates from the volume expansion
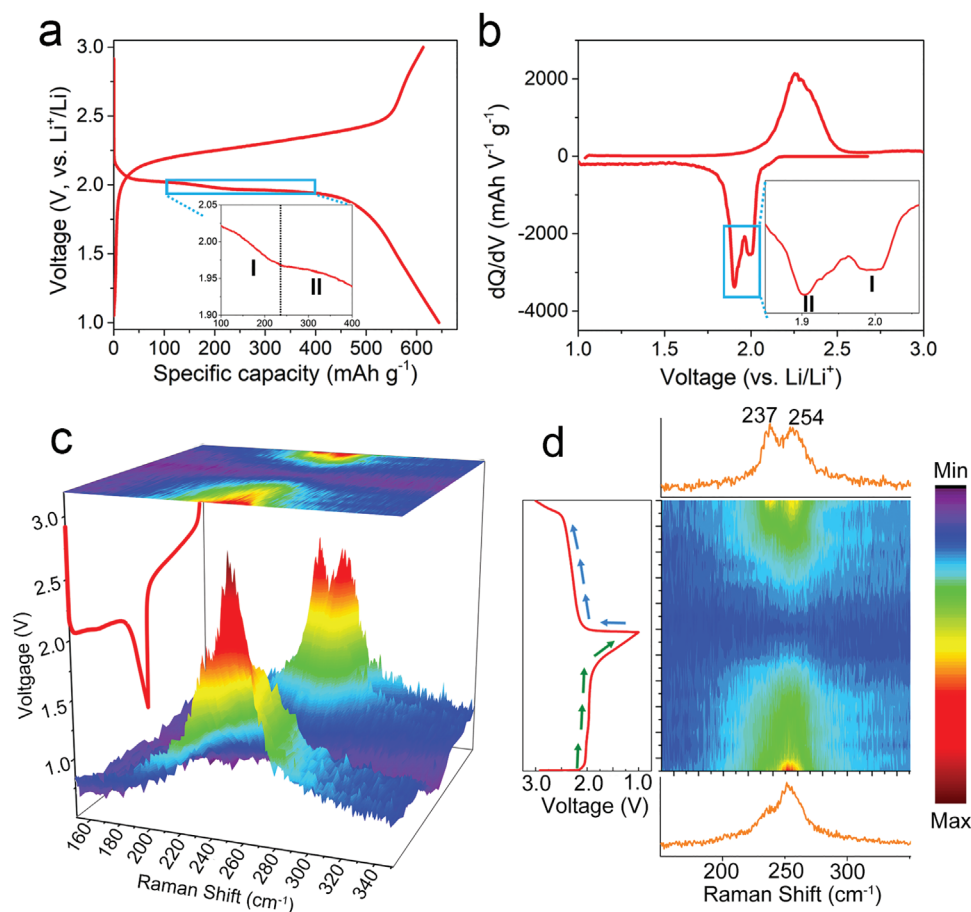
Figure 2. a) The typical discharge/charge profile of Se–LHC–C cathode at 50 mA g^{-1}, with enlarged discharge profile in the range of 1.90–2.05 V. b) The dQ/dV curve of Se–LHC–C cathode, with enlarged reduction peaks in the 1.85–2.05 V. c) 3D and d) contour plots of the in situ Raman spectra during initial discharge/charge process.

of the active material within cathode composites. No significant increase was observed during the charging process, implying that feasible charge carrier transfer can be maintained. To further identify and relate the dominant time constants in the impedance measurement to detailed electrochemical contributions, the impedance spectra were further analyzed using a semiquantitative distribution of relaxation times (DRT) method.[41] Four dominant peaks appear in the DRT result during discharge (Figure 3b), which are labeled as D1, D2, D3, and D4. The D1 peak at ultrahigh frequencies above 10^6 Hz is almost independent of the discharge state. This peak corresponds to the contact resistance at current collectors and electrode interfaces, and electrode particles.[42,43] The D2 and D3 peaks are associated with ion transport across the anode and cathode interface, respectively.[44] The D4 peak with the largest time constants (frequency below 0.1 Hz) is related to the solid-state diffusion (charge transfer process) of the Se cathode. The D2, D3, and D4 peaks are greatly affected by the state of discharge, especially D4 with the largest strength. By observing the changing trend, the D2 and D3 peaks gradually move toward lower frequency and their intensities continue to weaken initially, then both peaks become stable in the following discharge process. The intensity of the D4 peak greatly decreases at the beginning of discharge and also stabilizes afterward. The

change of D4 peak should be related to the lithiation state of Se cathode and indicates that two different lithiation processes of Se cathode leads to a different magnitude of charge transfer within cathodes. A more obvious change trend can be observed in the intensity color map of the discharge-dependent DRT curves in Figure 3c and Figure S15, Supporting Information. Similar to discharge, four obvious peaks can be observed in the DRT result during charge (Figure 3e). The C1 peak assigned to the contact impedance still remains unchanged during the whole process, which again demonstrates that close contact between particles can be maintained. Different from their counterparts in the discharge process, the C2, C3, and C4 peaks show opposite change trends in intensity, which increase gradually during charge (Figure 3e,f). Since the C4 peak is associated with the solid-state diffusion (charge transfer process) of the active cathode, the gradual change in the value of this peak indicates the continuous delithiation process, which differs from the case in the discharge process (lithiation).

The galvanostatic intermittent titration technique (GITT) was performed to study the lithiation/delithiation process by providing both thermodynamic and kinetic information of the battery system (**Figure 4**a). The cells were allowed to relax for 2 h after every 0.5 h discharge/charge at 50 mA g^{-1}. The open-circuit voltages can be obtained by extracting the voltages at

ADVANCED
SCIENCE NEWS

www.advancedsciencenews.com

ADVANCED
MATERIALS

www.advmat.de
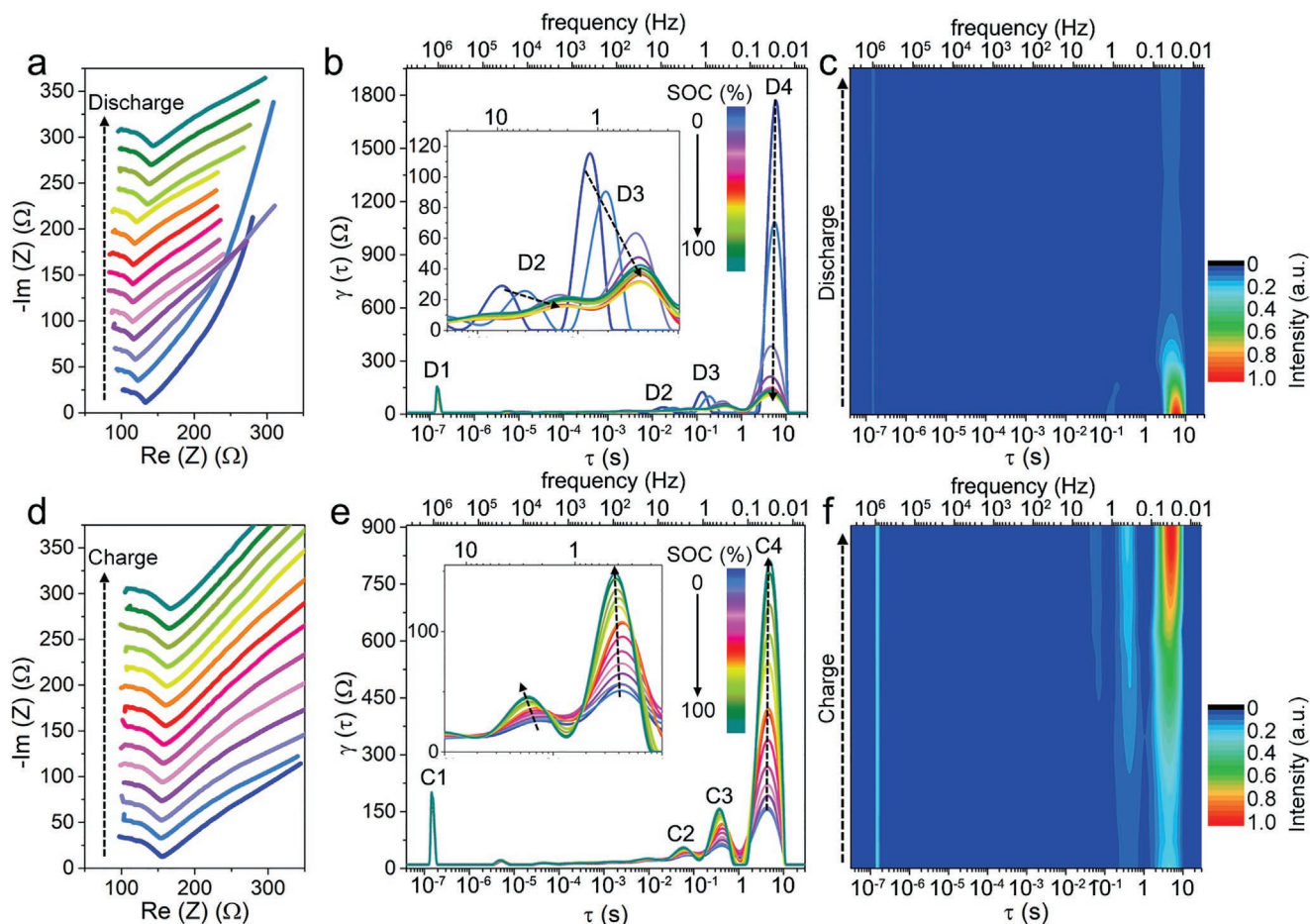
Figure 3. a) Impedance spectra of the Se–LHC–C/LHC/Li cell recorded after 0.5 h rest during discharge (cycled at 50 mA g^{-1} for 1 h). b) DRT calculated from EIS measurements at different states of discharge. c) 2D intensity color map of the discharge-dependent DRT curves in (b). d) Impedance spectra of the Se–LHC–C/LHC/Li cell recorded after 0.5 h rest during charge (cycled at 50 mA g^{-1} for 1 h). e) DRT calculated from EIS measurements at different states of charge. f) 2D intensity color map of the charge-dependent DRT curves in (e).

the end of the relaxation periods. The corresponding voltage hysteresis (Figure S16, Supporting Information) during the GITT tests shows smaller voltage change during the relaxation periods, in comparison to the previous report in a sulfide-based all-solid-state Li–Se system at room temperature.[10] Since the voltage hysteresis is related to the Ohmic voltage drop and reaction overpotential, a smaller hysteresis demonstrates more feasible reaction kinetics in the halide-based system. The apparent Li$^+$ diffusion coefficients (D_{Li}) calculated based on Fick's second law were around 10^{-11} cm^2 s^{-1} except the beginning of the discharge/charge process. This value is comparable to that of the liquid system, indicating similar Li insertion/extraction kinetics.

The pressure changes upon cycling were monitored through an in situ pressure measurement shown in Figure 4b. The net-pressure change (Δpressure) of the all-solid-state Se–LHC–C/LHC/Li cell is governed by the volume changes of the Se cathode. It can be seen that the pressure changes in a periodic manner depending on the degree of lithiation/delithiation of the Se cathode. The cell volume expands during the discharge process resulting in a net pressure of ≈0.5 MPa, which is comparable to the conventional cathode materials reports in sulfide-based all-solid-state systems.[45] Thus, to alleviate the

compressive stress and maintain interfacial contact, an external pressure of about 300 MPa was for the electrochemical performance tests of the all-solid-state Se–LHC–C/LHC/Li cell. In contrast, the electrochemical behavior without externally applied pressure is also shown in Figure S17, Supporting Information. Though the application of external pressure will burden the manufacturing design, it is widely used and important to ensure the good contact of solid particles and stable cycling performance in the all-solid-state cells in the current stage.

The morphologies and structures evolution of the Se–LHC–C cathode with pressure during the first discharge/charge process were characterized. As shown in Figure S18, Supporting Information, it gradually forms a film-like layer on the cathode surface during lithiation, which is caused by the volume expansion of the Se cathode. Uniform small particles are re-obtained at a fully delithiated state, while no obvious cracks are observed, which should benefit from the externally applied pressure of the cell. Figure 4c shows the differential capacity as a function of voltage (dQ/dV vs V) for all-solid-state Li–Se cell at 0.1 C. In the range of 20 cycles, the peak during the charge process almost remains stable. The intensity of discharge peaks during discharge slightly decreases after the

**ADVANCED
SCIENCE NEWS**

www.advancedsciencenews.com

**ADVANCED
MATERIALS**

www.advmat.de
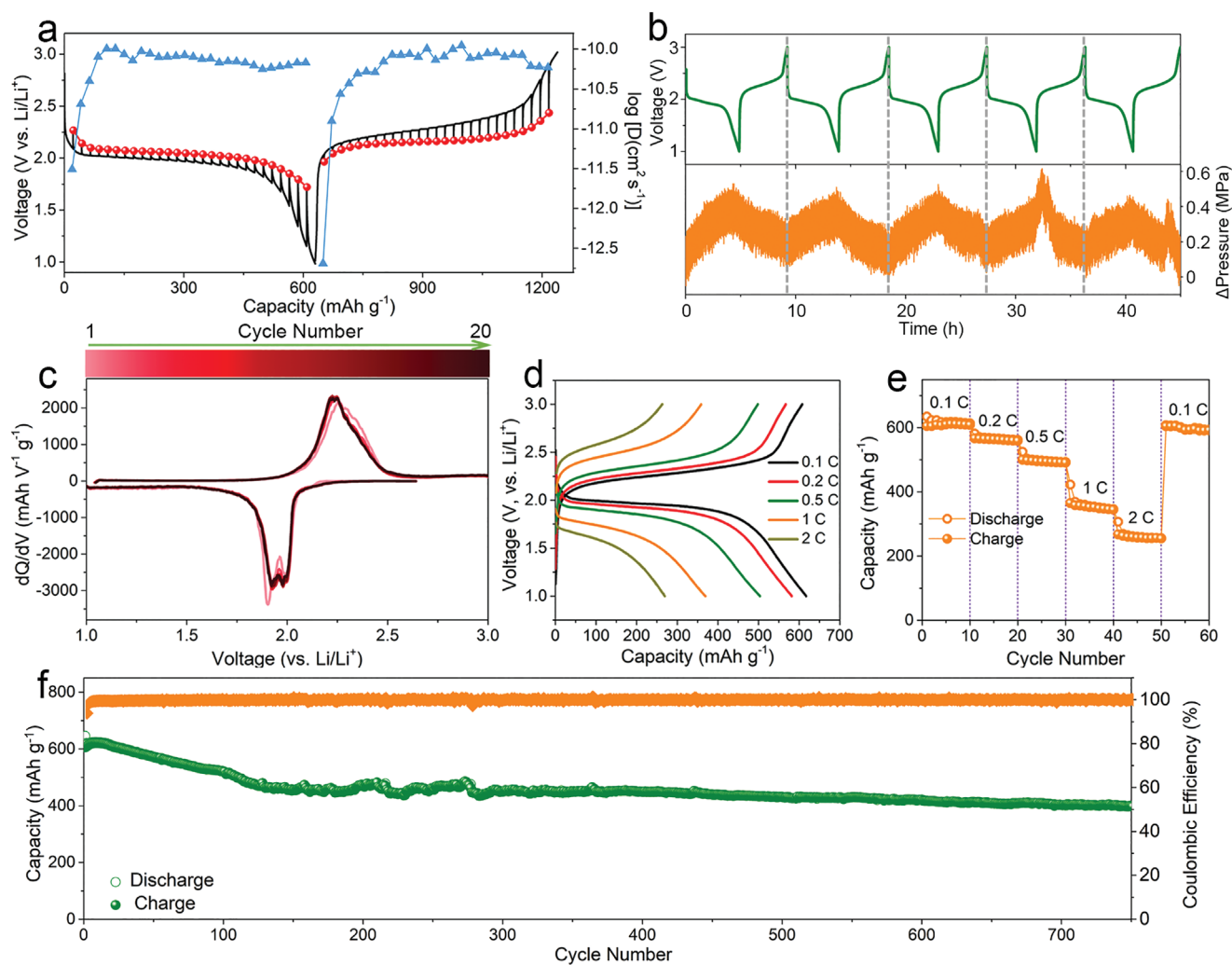
Figure 4. Electrochemical performance of the all-solid-state Se–LHC–C/LHC/Li cells at 25 °C. a) GITT of the Se–LHC–C/LHC/Li cell in the third cycle. 50 mA g^{-1} current pulses are used for 1 h increments followed by a 2 h relaxation. b) Discharge/charge profiles combined with the in situ cell pressure evolution of the Se–LHC–C/LHC/Li all-solid-state cell. c) dQ/dV curves of the Se–LHC–C/LHC/Li cell in the initial 20 cycles. d) Discharge/charge curves and e) cycling performance of the Se–LHC–C/LHC/Li cell at different rates (0.1, 0.2, 0.5, 1, and 2 C). f) Cycling performance and Coulombic efficiency of the Se–LHC–C/LHC/Li cell at 0.1 C.

initial cycles, while still overlapping with each other in the following cycles. The two well-maintained discharge peaks again prove the stepwise lithiation process of Se cathode in the halide-based solid-state system. The all-solid-state Li–Se cell also shows good rate capability as shown in Figure 4d,e. With increasing current density from 0.1 to 0.2, 0.5, 1, and 2 C, a reversible capacity of 615, 579, 502, 369, and 270 mAh g^{-1} is maintained, respectively. After reversing the current density back to 0.1 C, a reversible capacity of 597 mAh g^{-1} is recovered (Figure 4e). Figure 4f shows the cycling stability and Coulombic efficiency for 750 cycles. The Coulombic efficiency is higher than 99% after the initial cycle and gradually increases to over 99.9% after the tenth cycle, demonstrating the highly reversible performance of the cells. A reversible capacity of 402 mAh g^{-1} is retained at the 750th cycle, corresponding to a capacity degradation of 0.047% per cycle. The high performance of the cells indicates that halide SSEs are promising electrolytes for the Li–Se battery system.

Density functional theory (DFT) calculations were further performed to theoretically evaluate lithiation in the amorphous Se chains described above and to rationalize the two discharge plateaus observed in the halide system. There are indeed only three Se sites (i.e., Se0, Se1, and Se2, **Figure 5**a) of the amorphous Se chain. The calculated bond breaking and lithiation energies (ΔU) of the Se0–S1, Se0–Se2, and Se1–S2 bonds are −147.49, −328.74, and −143.07 kJ mol^{-1} (Figure 5b–d), respectively. The lithiation energy of Se0–Se1 and Se1–Se2 are similar, which are both much larger than that of Se0–Se2. Thus, the first discharge plateau around 2.0 V should be related to the bond breaking and lithiation of Se0–Se2 considering its lowest energy. Moreover, the Se0–Se2 bonds account for one-third of total Se sites within the structure. Correspondingly, the lithiation intermediate at the end of the first discharge plateau should be Li$_2$Se$_6$ (Figure 5e), which consists well with discharge capacity (≈205 mAh g^{-1}) during the lithiation process. Further lithiation of the intermediate phase results in the fully lithiated
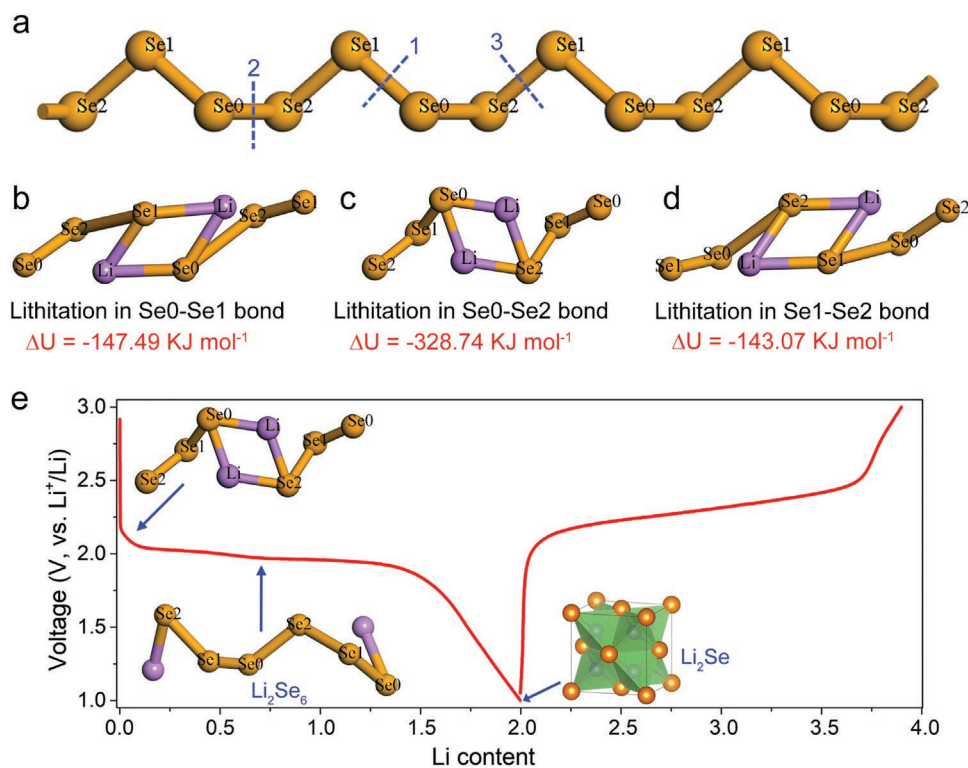
Figure 5. a) Structure of amorphous Se chain. b–d) DFT calculations for the Se—Se bond breaking and lithiation. e) The illustration of reaction pathways of the Se cathode in the solid system.

product of Li_2Se. As aforementioned, the Se–LHC–C cathode still undergoes two lithiation processes in the following cycles (Figure 4c) through the partial crystallization of Se after the first cycle. That's reasonable because the ordered or disordered state of the Se chain has little influence on its bond breaking and lithiation energy. In addition, it should be noted that there's no side reaction between halide SSE and Se (or lithiated Se) nor SSE decomposition enabled by its wide electrochemical stability window. Therefore, the lithiation mechanism of the Se cathode proposed here is its intrinsic lithiation behavior in the solid system. The failed observed discharge plateau in carbonate or sulfide electrolytes should be due to the sluggish reaction caused by the Se/electrolyte interface formation and electrolyte decomposition.

3. Conclusion

Through materials selection and system design, we have developed a highly stable and compatible all-solid-state Li–Se battery using a halide Li_3HoCl_6 as the inorganic solid electrolyte. This integrated solid-state Li–Se battery system effectively overcomes many of the issues which occur in conventional liquid and solid-based Li–Se cells, such as dissolution of Se, high instability, poor interfacial compatibility, and electrolyte–electrode decomposition. Owing to the high stability between the electrolyte and Se (or Li_xSe_y) species and intrinsic wide electrochemical stability window of the metal-halide electrolyte, a multistep reaction mechanism of the lithiation/delithiation process of Se cathode in solid was revealed. The electrochemical performance,

intrinsic thermodynamic lithiation/delithiation mechanism, and stability of the halide solid-state Li–Se battery system hold great promise for next-generation electronic devices with high energy density, long cycle life, and enhanced safety.

Supporting Information

Supporting Information is available from the Wiley Online Library or from the author.

Conflict of Interest

The authors declare no conflict of interest.

Data Availability Statement

The data that support the findings of this study are available from the corresponding author upon reasonable request.

Keywords

[1] A. Eftekhari, *Sustainable Energy Fuels* **2017**, *1*, 14.

[2] J. Sun, Z. Du, Y. Liu, W. Ai, K. Wang, T. Wang, H. Du, L. Liu, W. Huang, *Adv. Mater.* **2021**, *33*, 2003845.

[3] A. Abouimrane, D. Dambournet, K. W. Chapman, P. J. Chupas, W. Weng, K. Amine, *J. Am. Chem. Soc.* **2012**, *134*, 4505.

[4] J. Wang, S. Qu, R. Zhang, K. Yang, S. Zhang, R. G. Nuzzo, J. Nanda, P. V. Braun, *Energy Technol.* **2021**, *9*, 2100175.

[5] G.-L. Xu, J. Liu, R. Amine, Z. Chen, K. Amine, *ACS Energy Lett.* **2017**, *2*, 605.

[6] H. Tian, H. Tian, S. Wang, S. Chen, F. Zhang, L. Song, H. Liu, J. Liu, G. Wang, *Nat. Commun.* **2020**, *11*, 5025.

[7] W. P. Wang, J. Zhang, Y. X. Yin, H. Duan, J. Chou, S. Y. Li, M. Yan, S. Xin, Y. G. Guo, *Adv. Mater.* **2020**, *32*, 2000302.

[8] S. Lee, H. Lee, N. Ha, J. T. Lee, J. Jung, K. Eom, *Adv. Funct. Mater.* **2020**, *30*, 2000028.

[9] J. Zhao, W. Guo, Y. Fu, *Mater. Today Energy* **2020**, *17*, 100442.

[10] X. Li, J. Liang, X. Li, C. Wang, J. Luo, R. Li, X. Sun, *Energy Environ. Sci.* **2018**, *11*, 2828.

[11] Q. Zhang, L. Cai, G. Liu, Q. Li, M. Jiang, X. Yao, *ACS Appl. Mater. Interfaces* **2020**, *12*, 16541.

[12] S. Wang, Q. Bai, A. M. Nolan, Y. Liu, S. Gong, Q. Sun, Y. Mo, *Angew. Chem., Int. Ed.* **2019**, *58*, 8039.

[13] F. Han, Y. Zhu, X. He, Y. Mo, C. Wang, *Adv. Energy Mater.* **2016**, *6*, 1501590.

[14] G.-L. Zhu, C.-Z. Zhao, H. Yuan, B.-C. Zhao, L.-P. Hou, X.-B. Cheng, H.-X. Nan, Y. Lu, J. Zhang, J.-Q. Huang, *Energy Storage Mater.* **2020**, *31*, 267.

[15] T. K. Schwietert, V. A. Arszelewska, C. Wang, C. Yu, A. Vasileiadis, N. J. de Klerk, J. Hageman, T. Hupfer, I. Kerkamm, Y. Xu, *Nat. Mater.* **2020**, *19*, 428.

[16] G. F. Dewald, S. Ohno, M. A. Kraft, R. Koerver, P. Till, N. M. Vargas-Barbosa, J. Janek, W. G. Zeier, *Chem. Mater.* **2019**, *31*, 8328.

[17] T. Asano, A. Sakai, S. Ouchi, M. Sakaida, A. Miyazaki, S. Hasegawa, *Adv. Mater.* **2018**, *30*, 1803075.

[18] X. Li, J. Liang, J. Luo, M. N. Banis, C. Wang, W. Li, S. Deng, C. Yu, F. Zhao, Y. Hu, T.-K. Sham, L. Zhang, S. Zhao, S. Lu, H. Huang, R. Li, K. R. Adair, X. Sun, *Energy Environ. Sci.* **2019**, *12*, 2665.

[19] K. Wang, Q. Ren, Z. Gu, C. Duan, J. Wang, F. Zhu, Y. Fu, J. Hao, J. Zhu, L. He, C.-W. Wang, Y. Lu, J. Ma, C. Ma, *Nat. Commun.* **2021**, *12*, 4410.

[20] J. Liang, X. Li, S. Wang, K. R. Adair, W. Li, Y. Zhao, C. Wang, Y. Hu, L. Zhang, S. Zhao, *J. Am. Chem. Soc.* **2020**, *142*, 7012.

[21] L. Zhou, C. Y. Kwok, A. Shyamsunder, Q. Zhang, X. Wu, L. F. Nazar, *Energy Environ. Sci.* **2020**, *13*, 2056.

[22] K.-H. Park, K. Kaup, A. Assoud, Q. Zhang, X. Wu, L. F. Nazar, *ACS Energy Lett.* **2020**, *5*, 533.

[23] H. Kwak, D. Han, J. Lyoo, J. Park, S. H. Jung, Y. Han, G. Kwon, H. Kim, S. T. Hong, K. W. Nam, *Adv. Energy Mater.* **2021**, *11*, 2003190.

[24] J. Park, D. Han, H. Kwak, Y. Han, Y. J. Choi, K.-W. Nam, Y. S. Jung, *Chem. Eng. J.* **2021**, *425*, 130630.

[25] S. Y. Kim, K. Kaup, K.-H. Park, A. Assoud, L. Zhou, J. Liu, X. Wu, L. F. Nazar, *ACS Mater. Lett.* **2021**, *3*, 930.

[26] Z. Liu, S. Ma, J. Liu, S. Xiong, Y. Ma, H. Chen, *ACS Energy Lett.* **2020**, *6*, 298.

[27] X. Li, J. Liang, N. Chen, J. Luo, K. R. Adair, C. Wang, M. N. Banis, T.-K. Sham, L. Zhang, S. Zhao, S. Lu, H. Huang, R. Li, X. Sun, *Angew. Chem., Int. Ed.* **2019**, *58*, 16427.

[28] C. Wang, J. Liang, J. Luo, J. Liu, X. Li, F. Zhao, R. Li, H. Huang, S. Zhao, L. Zhang, *Sci. Adv.* **2021**, *7*, 1896.

[29] K. Kim, D. Park, H.-G. Jung, K. Y. Chung, J. H. Shim, B. C. Wood, S. Yu, *Chem. Mater.* **2021**, *33*, 3669.

[30] B. Zahiri, A. Patra, C. Kiggins, A. X. B. Yong, E. Ertekin, J. B. Cook, P. V. Braun, *Nat. Mater.* **2021**, *20*, 1392.

[31] S. Zhang, F. Zhao, S. Wang, J. Liang, J. Wang, C. Wang, H. Zhang, K. Adair, W. Li, M. Li, *Adv. Energy Mater.* **2021**, *11*, 2100836.

[32] L. Zhou, T.-T. Zuo, C. Y. Kwok, S. Y. Kim, A. Assoud, Q. Zhang, J. Janek, L. F. Nazar, *Nat. Energy* **2022**, *7*, 83.

[33] J. Liang, X. Li, K. R. Adair, X. Sun, *Acc. Chem. Res.* **2021**, *54*, 1023.

[34] Y. Zhang, Y. Sun, L. Peng, J. Yang, H. Jia, Z. Zhang, B. Shan, J. Xie, *Energy Storage Mater.* **2019**, *21*, 287.

[35] X. Li, J. Liang, J. Luo, C. Wang, X. Li, Q. Sun, R. Li, L. Zhang, R. Yang, S. Lu, *Adv. Mater.* **2019**, *31*, 1808100.

[36] L. Ye, X. Li, *Nature* **2021**, *593*, 218.

[37] W. Ji, D. Zheng, X. Zhang, T. Ding, D. Qu, *J. Mater. Chem. A* **2021**, *9*, 15012.

[38] S. Ohno, C. Rosenbach, G. F. Dewald, J. Janek, W. G. Zeier, *Adv. Funct. Mater.* **2021**, *31*, 2010620.

[39] J. Yi, L. Chen, Y. Liu, H. Geng, L.-Z. Fan, *ACS Appl. Mater. Interfaces* **2019**, *11*, 36774.

[40] V. V. Poborchii, A. V. Kolobov, K. Tanaka, *Appl. Phys. Lett.* **1998**, *72*, 1167.

[41] T. H. Wan, M. Saccoccio, C. Chen, F. Ciucci, *Electrochim. Acta* **2015**, *184*, 483.

[42] X. Chen, L. Li, M. Liu, T. Huang, A. Yu, *J. Power Sources* **2021**, *496*, 229867.

[43] P. Gargh, A. Sarkar, Y. H. Lui, S. Shen, C. Hu, S. Hu, I. C. Nlebedim, P. Shrotriya, *J. Power Sources* **2021**, *485*, 229360.

[44] P. S. Sabet, D. U. Sauer, *J. Power Sources* **2019**, *425*, 121.

[45] S. Wang, M. Tang, Q. Zhang, B. Li, S. Ohno, F. Walther, R. Pan, X. Xu, C. Xin, W. Zhang, *Adv. Energy Mater.* **2021**, *11*, 2101370.